A Model-Based Iterative Algorithm for Dual-Energy X-Ray CT Reconstruction

Ruoqiao Zhang, Jean-Baptiste Thibault, *Member*, *IEEE*, Charles A. Bouman, *Fellow*, *IEEE*, Ken D. Sauer, *Member*, *IEEE*, and Jiang Hsieh, *Senior Member*, *IEEE*

***Abstract*—Recent developments in dual-energy X-ray CT have shown a number of benefits over standard CT for object separation, contrast enhancement, artifact reduction, and material composition assessment. As with traditional CT, model-based iterative approaches to reconstruction offer the opportunity to reduce noise and artifacts in dual energy reconstructions. However, previous approaches to model-based dual energy reconstruction have not fully modeled the statistical dependencies in the material-decomposed data. In this paper, we present a method for model-based iterative reconstruction which accounts for both the statistical dependency in the material decomposed sinogram components, and fast-switching approaches to dual-energy sampling. Our method also incorporates a positivity constraint in the space domain which accurately accounts for the true physical constraint of positive X-ray attenuation and is computationally simple to implement. Both phantom and clinical results show that the proposed model produces images which compare favorably to FBP in overall image quality.**

I. Introduction

Acquiring X-ray CT exposures at two distinct energy levels can help distinguish different material types, which is of great importance in disease diagnosis and security inspection. Dual-energy CT reconstruction typically works by reconstructing two density maps for two basis materials. The cross-sectional attenuation map at any given energy can then be computed as a linear combination of the two material density maps [1].

A typical approach to dual-energy reconstruction works by first transforming the low and high energy photon counts into quantities that are proportional to the integral of the material density for two basis materials. This material-decomposed sinogram can then be directly reconstructed using FBP to form the material density maps in image space. The transformation from photon counts to integral projections is performed by a material-decomposition function, which can then be experimentally measured through a scanner calibration procedure. However, the processes of applying this material-decomposition function changes the statistics of the measured data, which results in reconstructions that have statistically correlated noise properties.

Statistical iterative methods have the natural advantage that they can explicitly build data statistics into the dual-energy problem description, and account for the significant changes occurring during material decomposition. Some statistical approaches [2], [3] have been proposed from a rigorous theoretical perspective to reconstruct the material images directly from the low- and high-energy projections. On the other hand, Model-Based Iterative Reconstruction (MBIR), which views the reconstruction problem as the solution of a Maximum *A Posteriori* (MAP) estimation formulation, has been found to be very effective in reconstruction of single-energy CT images [4], [5].

In this paper, we propose an approach for applying MBIR to the dual-energy X-ray CT problem. Our approach explicitly accounts for the correlation of scanner noise caused by the material-decomposition process, and it also allows for accurate modeling of data collected using kV switching techniques, in which low and high energy measurements are used at alternating views. The MBIR approach incorporates a prior model that accounts for the separation into materials, and includes a simple positivity constraint that accurately accounts for the true physical constraint of positive X-ray attenuation.

II. Problem Formulation and Proposed Solution

A. Problem Formulation

The linear attenuation coefficient $x(E)$ of any material as a function of energy E can be expressed as a linear combination of mass attenuation coefficients of two basis materials [1]. Without loss of generality, in this paper we choose the basis materials as water and iodine. Then the relationship can be described as

$$x_j(E) = m_j \cdot \mu^T(E), \tag{1}$$

where j is the index of the voxel, $m_j \triangleq [m_{j,W},\ m_{j,I}]$ represents the water-equivalent and iodine-equivalent densities at voxel j and $\mu(E) \triangleq [\mu_{_W}(E),\ \mu_{_I}(E)]$ represents the known mass attenuation coefficients for water and iodine. The task is to reconstruct the material densities from the measurements obtained from dual-energy acquisition.

Let $m \in \Re^{N\times 2}$ represent the reconstructed images for the selected material basis pair, where each row is given by $m_j = [m_{j,W},\ m_{j,I}]$. Furthermore, let $y \in \Re^{M\times 2}$ be the set of dual-energy sinogram measurements, where each row given by, $y_i = [y_{i,l},\ y_{i,h}]$, specifies the low and high energy measurements for the i^{th} projection.

Then the reconstruction problem can be formulated as computing the MAP estimate given by

$$\hat{m} = \arg\max_{m\in\Omega^N} \{\log P(y|m) + \log P(m)\}, \tag{2}$$

This work was supported by GE Healthcare.

R. Zhang and C. A. Bouman are with the School of Electrical and Computer Engineering, Purdue University, West lafayette, IN 47907-0501 USA (email: zhang393@purdue.edu; bouman@ecn.purdue.edu).

J.-B. Thibault and J. Hsieh are with GE Healthcare Technologies, Waukesha, WI 53188 USA (email: jean-baptiste.thibault@med.ge.com; jiang.hsieh@med.ge.com).

K. D. Sauer is with the Department of Electrical Engineering, University of Notre Dame, Notre Dame, IN 46556-5637 USA (email: sauer@nd.edu).

where $P(y|m)$ is the conditional distribution of y given m, $P(m)$ is the prior distribution of m, and Ω is the constrained set for each voxel.

B. Forward Model

Let $p \in \Re^{M\times 2}$ be the forward projection of the material reconstruction, with its i^{th} row given by

$$p_i \triangleq \left[\int\limits_{ray\ i} m_{*,_W}(r)dr, \quad \int\limits_{ray\ i} m_{*,_I}(r)dr \right] \tag{3}$$

Then p can be expressed as $p = Am$ where A is the forward projecting matrix for the CT system.

Furthermore, we may define a vector-valued function $h_i : \Re^2 \rightarrow \Re^2$, which transfers the material projections to the expected photon attenuation along the i^{th} ray, as

$$h_i(p_i) \triangleq -\log\left(\int\limits_{\mathbb{R}} s_i(\mathcal{E}) \exp\left\{ -p_i \mu^T(\mathcal{E}) \right\} d\mathcal{E} \right), \tag{4}$$

where $\mathcal{E}$ denotes the X-ray photon energy, vector $s_i(\mathcal{E})$ represents the two normalized source/detector spectra for the i^{th} ray. Assuming h_i is invertible, the corresponding inverse function h_i^{-1} is defined as

$$h_i^{-1}(h_i(p_i)) \triangleq p_i \ . \tag{5}$$

Assume that for each detector, a measurement is made of the photon counts for both the low and high energy case. Then we can compute the associated low and high attenuation measurement as

$$y_i \triangleq \left[-\log\left(\frac{\lambda_{i,l}}{\lambda_{i,o,l}} \right), -\log\left(\frac{\lambda_{i,h}}{\lambda_{i,o,h}} \right) \right], \tag{6}$$

where $\lambda_{i,l}$ and $\lambda_{i,h}$ represent the measured photon counts along the i^{th} ray at low and high energies, respectively, and $\lambda_{i,o,l}$ and $\lambda_{i,o,h}$ represent the expected air-scanned photon rate. Then y_i has approximate mean $h_i(p_i)$ and approximate inverse covariance W_i as

$$W_i = diag\left\{ w_{i,l},\ w_{i,h} \right\}. \tag{7}$$

The diagonal elements $w_{i,l}$ and $w_{i,h}$ give the inverse variances of $y_{i,l}$ and $y_{i,h}$ respectively. Zero off-diagonal entries come from the assumption that the incident rays with different energy levels are mutually independent. The values of $w_{i,l}$ and $w_{i,h}$ can be estimated by using the photon count measurement λ_i [6], [7], as

$$w_{i,l} = \frac{\lambda_{i,l}^2}{\lambda_{i,l} + \sigma_e^2}, \tag{8}$$

$$w_{i,h} = \frac{\lambda_{i,h}^2}{\lambda_{i,h} + \sigma_e^2}, \tag{9}$$

where σ_e^2 represents the variance of electronic noise in the data acquisition [8]. The log-likelihood term can then be approximated by a second-order Taylor series expansion using a Poisson-Gaussian noise model [6], [7], which yields the quadratic expression:

$$\begin{aligned} &-\log P(y|m) \\ \approx &\frac{1}{2}\sum_i \left(y_i - h_i(A_{i,*}m)\right) W_i \left(y_i - h_i(A_{i,*}m)\right)^T + f(y), \end{aligned} \tag{10}$$

where $f(y)$ is a function depending on data y only. Define $\hat{p}_i$ as an estimate of the material projection p_i, which is obtained via the h_i^{-1} function,

$$\hat{p}_i \triangleq h_i^{-1}(y_i). \tag{11}$$

Then by a first order approximation, the likelihood term can be written as

$$-\log P(y|m) \approx \frac{1}{2}\sum_i \left(\hat{p}_i - A_{i,*}m\right) B_i \left(\hat{p}_i - A_{i,*}m\right)^T, \tag{12}$$

where the weighting matrix B_i is given by

$$B_i \triangleq [\nabla h_i^{-1}(y_i)]^{-1} W_i [\nabla h_i^{-1}(y_i)]^{-T}. \tag{13}$$

Each B_i is a 2×2 symmetric matrix which represents the inverse covariance of the estimated material projections $\hat{p}_i$. The off-diagonal entries of B_i provide information about the correlation between the calculated projections of distinct materials.

This formulation also works for the fast kVp switching data acquisition mode, in which the effective source voltage changes from view to view. In this case, each projection only contains one of the low- or high-kV measurements. So if a low measurement is made, then $w_{i,h} = 0$, and if a high measurement is made, then $w_{i,l} = 0$. The missing components for the values of y_i are then computed by interpolation. However, these interpolated values are only used to compute the gradient $\nabla h_i^{-1}(y_i)$, which consequently only have a small effect the value of B_i. Moreover, the matrix B_i is always rank deficient in this case, with a zero eigenvalue in the direction of the missing information.

In practice, the h_i^{-1} can be the same material decomposition function used in FBP reconstruction, and it can be empirically measured from the physical system.

C. Prior Model

We employ a Markov random field (MRF) as our prior model with the form

$$-\log P(m) = \sum_{s\in\{W,I\}} \sum_{\{j,k\}\in\mathcal{C}} b_{jk,s}\rho(m_{j,s} - m_{k,s}), \tag{14}$$

where s is the index of material type, $\mathcal{C}$ represents the set of all neighboring voxel pairs, $b_{jk,s}$ are regularization weights and $\rho(.)$ is the potential function. Our particular choice of penalty here is the q-generalized Gaussian MRF (q-GGMRF) [4]:

$$\rho(\Delta) = \frac{|\Delta|^p}{1 + |\Delta/c|^{p-q}}. \tag{15}$$

with $1 < q \leq p \leq 2$, which guarantees strict convexity and therefore global convergence of the cost function. The parameter c balances the performance between noise reduction and edge preservation [4]. We choose here to perform this regularization independently on each of the material density images.

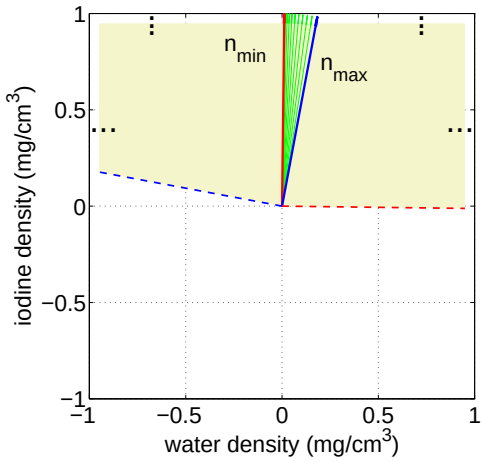

Fig. 1. This figure illustrates the feasible values of a pixel $m_j = [m_{j.W}, m_{j,I}]$. The set is formed by the intersection of only two half planes, one defined by n_{max} and the other by n_{min}.

D. Constrained Optimization

An important physical constraint to the solution is that the attenuation at every energy must be non-negative. More precisely for all $E \in [40, 140]$ keV, we know that

$$x_j(E) = m_j \cdot \mu^T(E) \geq 0 \ , \tag{16}$$

where the photon energy range [40, 140] keV is of particular interest for medical imaging and is above the k-edge of iodine. This constraint is then equivalent to the constraint that

$$m_j \cdot n^T(E) \geq 0 \ , \tag{17}$$

where $n(E) = \frac{\mu(E)}{||\mu(E)||}$ is the normalized mass attenuation vector. The constraint set is then given by $m_j \in \Omega$ where

$$\Omega = \cap_{E\in[40,140]}\{m_j \in \Re^2 : m_j \cdot n^T(E) \geq 0\} \ . \tag{18}$$

So Ω is formed by the intersection of an infinite number of half planes. However, the form of Ω can be dramatically simplified by noticing that the direction of $n(E)$ moves continuously with E, therefore the constraint can be represented much more simply by the intersection of two planes corresponding to the minimum and maximum values of $n(E)$ as n_{min} and n_{max}, with

$$\Omega = \left\{m : m_j \cdot n_{\min}^T \geq 0 \text{ and } m_j \cdot n_{\max}^T \geq 0\right\} . \tag{19}$$

The constraint set and the associated vectors are illustrated graphically in Fig. 1.

Combining the log likelihood in (12) and the prior in (14) with the above constraints, the MAP estimate of m can be obtained by solving the following constrained optimization:

$$\hat{m} = \arg \min_{m\in\Omega^N} \left\{ \frac{1}{2} \sum_i \left(\hat{p}_i - A_{i,*}m\right) B_i \left(\hat{p}_i - A_{i,*}m\right)^T + \sum_{s\in\{W,I\}} \sum_{\{j,k\}\in\mathcal{C}} b_{jk,s}\rho(m_{j,s} - m_{k,s}) \right\} . \tag{20}$$

We use iterative coordinate descent (ICD) algorithm with an FBP initial condition to solve the problem in (20), and with each ICD voxel update, we compute the exact solution to the constrained voxel update with the Karush-Kuhn-Tucker (KKT) conditions.

TABLE I
COMPARISON OF FBP AND MBIR FOR MEASUREMENT OF NOISE AND IN-PLANE MTF, FOR THE IMAGES IN FIG. 2. THE 10% MTF IS CHOSEN SINCE IT GENERALLY REPRESENTS THE VISUAL RESOLUTION OF THE IMAGE.

	Noise Std. Dev. (mg/cc)		10% MTF (lp/cm)	
	FBP	MBIR	FBP	MBIR
Water	21.21	9.68	6.15	11.80
Iodine	0.60	0.38	5.81	10.59
70keV Mono	14.18	13.69	6.60	11.70

III. RESULTS

In this section, we apply the dual-energy MBIR algorithm to both phantom and clinical reconstructions. Data is acquired on a Discovery CT750 HD scanner (GE Healthcare, WI) in dual-energy fast switching acquisition mode, rapidly alternating source voltage between 80 kVp and 140 kVp from view to view in 540 mAs. Each reconstructed 512×512 axial image has a prescribed thickness of 0.625mm. The reconstructed pixel value represents the water-equivalent or iodine-equivalent densities in units of mg/cm^3. The prior parameters are empirically chosen to be p = 2.0, q = 1.2, and c = 10. We will compare our method with a generic FBP method with a standard reconstruction filter kernel, which improves the FBP image quality via a correlation-based noise management [9]. Our method has not been optimized to yield a particular desired image quality performance.

Fig. 2 presents reconstructions of a GE Performance Phantom with 984 views per rotation for each kVp with pitch 0.938:1. As shown in the figures, MBIR creates smoother texture over FBP in flat regions. Fig. 3 shows the improvement in visual resolution brought by MBIR in the monochromatic image. Quantitative measurements also indicate that MBIR has the ability to improve the in-plane resolution with reduced noise over FBP, as illustrated in Table I.

Fig. 4 shows reconstructions of a clinical scan of the abdomen with 984 views per rotation for each kVp at a helical pitch of 0.984:1. By visual comparison to FBP, MBIR improves the water image by reducing noise and enhancing the overall contrast. The bone structures in the MBIR images exhibit less blooming and sharper edges than FBP, and the texture of the liver area is also improved. Some small lesions in the liver area and some fine structures are also enhanced in the MBIR images compared to the FBP images. The overall contrast enhancement by MBIR can also be observed in the monochromatic images. These results illustrate some potential diagnostic benefits of iterative reconstruction from dual-energy CT data.

IV. CONCLUSION

In this paper, we have presented a model-based iterative reconstruction approach for dual-energy X-ray CT reconstruction. The method combines a forward model to account for correlation between material decomposed projections with

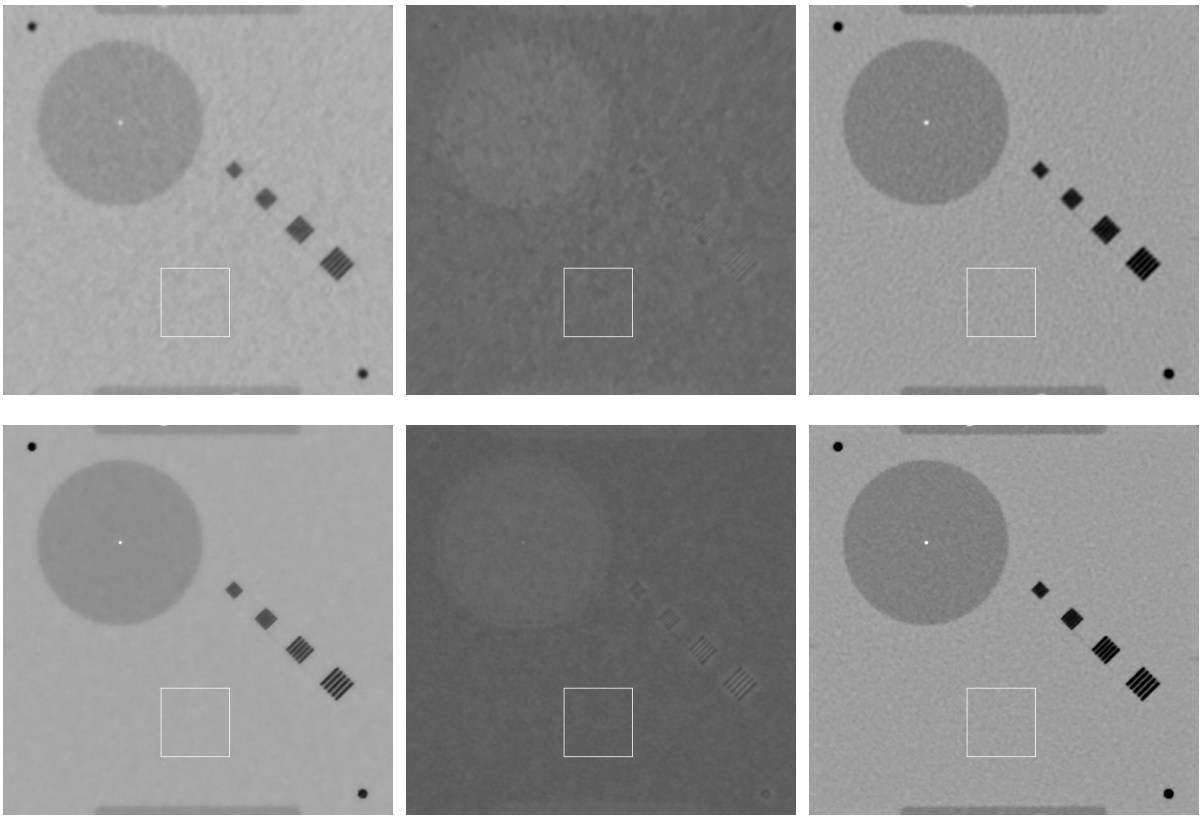

Fig. 2. Comparison of generic FBP vs MBIR performance on a GE Performance Phantom. All the images represent the same imaging plane in the 3D volume. Top left: FBP water image; top middle: FBP iodine image; top right: 70keV monochromatic FBP image. Bottom left: MBIR water image; bottom middle: MBIR iodine image; bottom right: 70keV monochromatic MBIR image. Display window for the water images: WW 1600mg/cm^3 and WL 900mg/cm^3; for iodine images: WW 40mg/cm^3 and WL 3mg/cm^3; for mono images: WW 1000HU and WL 0HU. The monochromatic image at a particular photon energy is generated by linearly combining water and iodine images with the corresponding mass attenuation coefficients at the given photon energy, according to equation in (1). The white box in the image indicates the region where the noise standard deviation is evaluated.

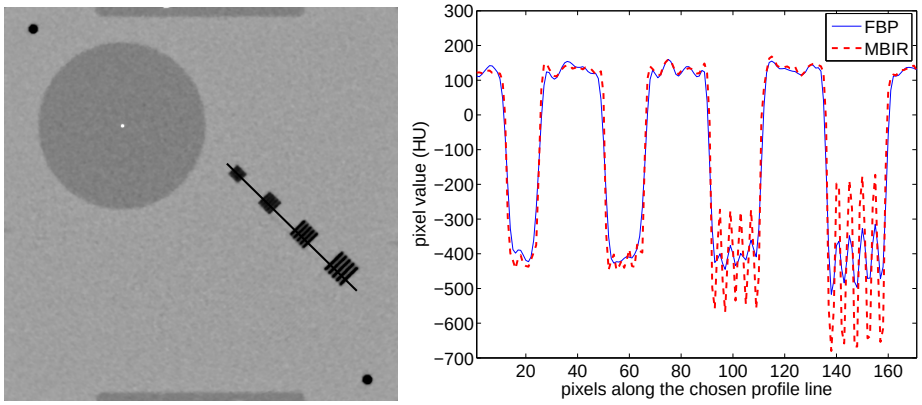

Fig. 3. Profile plot across the resolution bars on a GE Performance Phantom for FBP and MBIR images. Image on the LHS indicates the location of the profile line, which passes through the resolution bars perpendicularly. Image on the RHS shows the pixel values along that particular line in FBP (blue) and MBIR (red) images. It can be seen in the figure that the spikes in the MBIR image are much more enhanced than those in the FBP image, which makes the resolution bars more spatially separable.

MRF regularization, and features an additional physical constraint over the reconstructed linear attenuation coefficients. The proposed method has better performance than FBP in terms of noise reduction and spatial resolution. Further investigation will assess how to further improve material separation performance and investigate potential clinical benefits.

REFERENCES

[1] R. Alvarez and A. Macovski, "Energy-selective reconstructions in X-ray computerized tomography," *Med. Phys.*, vol. 21, no. 5, pp. 733–744, 1976.

[2] J. Fessler, I. Elbakri, P. Sukovic, and N. Clinthorn, "Maximum-likelihood dual-energy tomographic image reconstruction," in *Proc. SPIE4684, Medical Imaging 2002: Image Proc.*, vol. 1, 2002, pp. 38–49.

[3] J. O'Sullivan and J. Benac, "Alternating minimization algorithms for

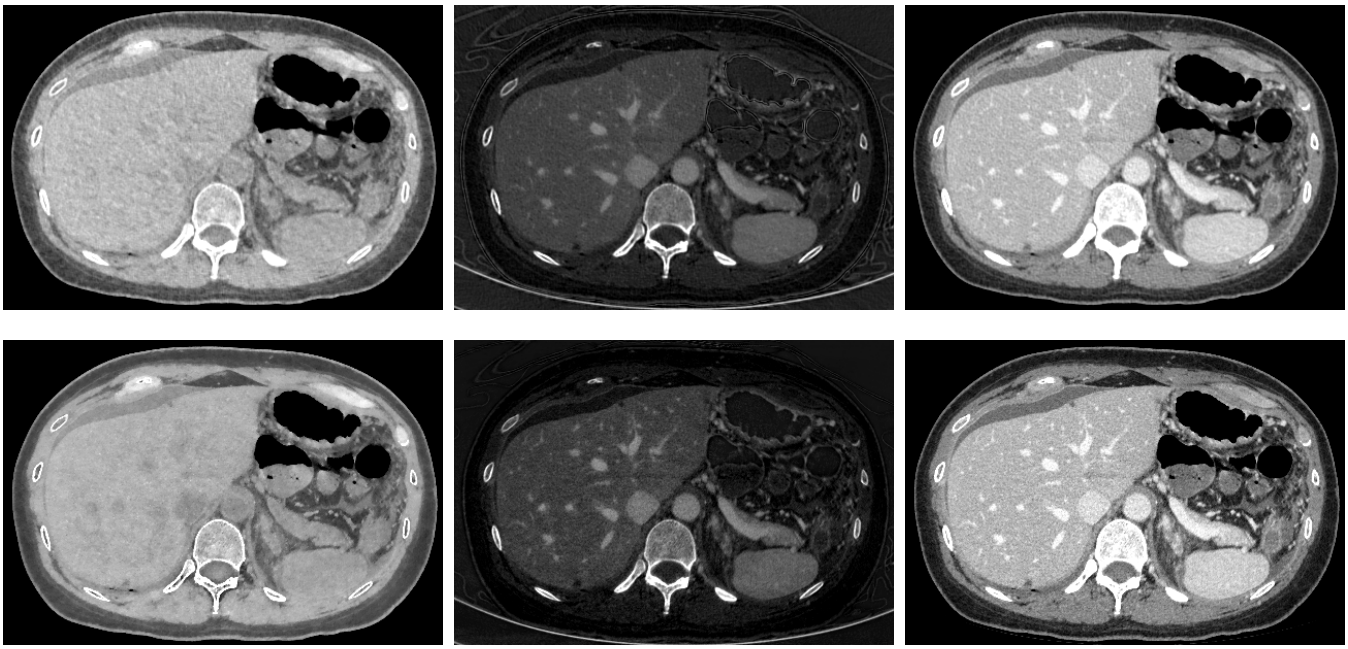

Fig. 4. Comparison of generic FBP vs MBIR performance on an abdominal clinical scan. All the images represent the same imaging plane in the 3D volume. Top left: FBP water image; top middle: FBP iodine image; top right: 70keV monochromatic FBP image. Bottom left: MBIR water image; bottom middle: MBIR iodine image; bottom right: 70keV monochromatic MBIR image. Display window for the water images: WW 300mg/cm^3 and WL 1000mg/cm^3; for iodine images: WW 17.5mg/cm^3 and WL 7.5mg/cm^3; for mono images: WW 400HU and WL 40HU.

transmission tomography," *IEEE Trans. on Medical Imaging*, vol. 26, no. 3, pp. 283–297, Mar. 2007.

[4] J.-B. Thibault, K. Sauer, J. Hsieh, and C. Bouman, "A three-dimensional statistical approach to improve image quality for multislice helical CT," *Med. Phys.*, vol. 34, no. 11, pp. 4526–4544, 2007.

[5] Z. Yu, J.-B. Thibault, C. Bouman, K. Sauer, and J. Hsieh, "Fast model-based X-ray CT reconstruction using spatially nonhomogeneous ICD optimization," *IEEE Trans. on Image Processing*, vol. 20, no. 1, pp. 161–175, January 2011.

[6] C. Bouman and K. Sauer, "A unified approach to statistical tomography using coordinate descent optimization," *IEEE Trans. on Image Processing*, vol. 5, no. 3, pp. 480–492, March 1996.

[7] K. Sauer and C. Bouman, "A local update strategy for iterative reconstruction from projections," *IEEE Trans. on Signal Processing*, vol. 41, no. 2, pp. 534–548, February 1993.

[8] J.-B. Thibault, C. Bouman, K. Sauer, and J. Hsieh, "A recursive filter for noise reduction in statistical tomographic imaging," in *Proc. SPIE/IS&T Symp. Comput. Imag. IV*, vol. 6065, San Jose, CA, Jan. 16-18, 2006.

[9] W. Kalendar, E. Klotz, and L. Kostaridou, "An algorithm for noise suppression in dual energy CT material density images," *IEEE Trans. on Medical Imaging*, vol. 7, no. 3, pp. 218–224, Sep. 1988.